New complex G-matrix interactions derived from two- and three-body forces and application to proton-nucleus elastic scattering

T. Furumoto[*]
Department of Physics, Osaka City University, Osaka 558-8585, Japan

Y. Sakuragi[†]
Department of Physics, Osaka City University, Osaka 558-8585, Japan, and RIKEN Nishina Center, RIKEN, Wako, Saitama 351-0198, Japan

Y. Yamamoto[‡]
Physics Section, Tsuru University, Tsuru, Yamanashi 402-8555, Japan

(Received 28 May 2008; published 14 October 2008)

A new type of complex G-matrix interactions including the effect of three-body nucleon-nucleon (NN) force is proposed and applied to the folding-model calculation of proton-nucleus elastic scattering at $E_p = 65 \sim 200$ MeV for ^{12}C, ^{40}Ca, ^{90}Zr, and ^{208}Pb target nuclei. All the measured cross sections and analyzing powers are well reproduced by the folding potentials with the new complex G-matrix interaction when the effect of three-body force (TBF) is included so as to give the reasonable saturation property. The inclusion of TBF largely reduces the strength of real-central component of folding potential at middle and short distances. The TBF effect is clearly observed in drastic improvements of analyzing powers at forward angles, which is, however, due to the TBF effect on the real-central potentials, not to the direct effects on the spin-orbit potentials. The calculated folding potential is shown to be very sensitive to the difference of neutron-density profile of the target nucleus.

DOI: 10.1103/PhysRevC.78.044610 PACS number(s): 21.30.−x, 21.65.−f, 24.10.Ht, 25.40.Cm

I. INTRODUCTION

It is a long-standing and fundamental subject to understand nucleon-nucleus (NA) and nucleus-nucleus (AA) interactions microscopically starting from the basic nucleon-nucleon (NN) interaction. Because, in general, this corresponds to solving a very complicated nuclear many-body problem in nuclear reactions, one needs to rely on an approximate but realistic and reliable approach to this goal. The folding model approach based on the lowest-order Brueckner theory will be one of such approaches. In the Brueckner theory, the so-called G-matrix is derived from a free-space NN interaction by solving the Bethe-Goldstone (BG) equation in nuclear matter of uniform nucleon density. The G-matrix is density-dependent due to the many-body effects such as the Pauli exclusion principle and the binding effect and considered to be the effective NN interaction in nuclear medium. When the BG equation is solved under the scattering boundary condition, the obtained G-matrix is complex, having real and imaginary parts, and dependent not only on the density but also on the energy of the incident nucleon. The folding model converts this G-matrix interaction in uniform nuclear matter into interactions between finite nuclear systems, i.e., nucleon-nucleus (NA) or nucleus-nucleus (AA) ones, on the basis of the local-density approximation (LDA). In other words, the G-matrix folding model is one of the microscopic model to construct complex optical potentials for NA or AA system starting from the underlying NN interaction. The G-matrix folding model for nucleon-nucleus optical potentials has a long history [1–9], where various kind of G-matrix interactions were proposed and applied to the analyses of nucleon-nucleus elastic scattering more or less successfully. In derivations of these G-matrix interactions, the adopted NN interaction models are different from each other.

It is well known that the empirical saturation point in nuclear matter (the binding energy per nucleon $E/A \approx 16$ MeV at a saturation density $\rho_0 \approx 0.17$ fm^{-3}) cannot be reproduced with any two-body NN interaction in the lowest-order Brueckner theory (G-matrix approximation). Then, one needs to introduce a three-body force to reproduce the nuclear saturation properties, which is indispensable to derive reliably the equation of state (EOS) and the incompressibility of high-density nuclear matter.

The importance of three-body force (TBF) is widely understood in nuclear structure calculations. In nuclear reaction studies, however, the role of TBF has not been well established, particularly in nucleon-nucleus elastic scattering. This is partly due to the fact that the elastic-scattering observables are given by asymptotic phase shifts of the scattering wave functions that are not very sensitive to the potential depth in nuclear interior where nucleon density is close to the saturation value ρ_0 and considerable TBF effects are expected.

As for the nucleus-nucleus (AA) system, the local density in overlap region $\rho_1 + \rho_2$ may exceed the nuclear-matter saturation density ρ_0 and could reach about twice the saturation density. In such a high-density region, one may expect a clear evidence of the TBF effect. However, all the existing G-matrix

[*]furumoto@ocunp.hep.osaka-cu.ac.jp
[†]sakuragi@ocunp.hep.osaka-cu.ac.jp
[‡]yamamoto@tsuru.ac.jp

interactions applied so far to the nucleon-nucleus (NA) scattering problems were only designed for densities below the saturation density ρ_0 with use of two-body NN interactions only. In the NA system, the local density does not exceed the saturation density and, hence, one needed not calculate G matrices up to higher densities. Therefore, the existing G-matrix interactions cannot directly be applied to AA scattering and, so far, two alternative prescriptions have been used in application to AA systems.

The first one is to introduce a phenomenological density dependence by hand so as to simulate the density dependence of original G matrix in low-density regions below the saturation density and extend it to higher-density regions by assuming a suitable functional form for the density dependence (such as DDM3Y [10]) so as to be consistent with the empirical EOS of nuclear matter [11,12] (In these cases, however, only the real part of G matrix is used in the folding calculation of AA optical potential and the imaginary part is treated in a completely phenomenological way.) The other prescription is to define a local density by an averaged value $(\rho_1 + \rho_2)/2$ instead of a sum of two densities $\rho_1 + \rho_2$ (the frozen-density prescription) so that local densities do not exceed the saturation density. However, this prescription apparently underestimate the local density of nucleus-nucleus system in overlap configurations, which leads to too deep potential strength at short distances and, hence, one needs to significantly reduce the potential strength [13]. Therefore, this prescription may not bring about the expected effects of three-body force in such situations. However, the former prescription is known to be quite successful in reproducing the nuclear-rainbow scattering and related refractive-scattering phenomena observed in light heavy-ion scattering such as $^{16}\mathrm{O} + {}^{16}\mathrm{O}$ and $^{16}\mathrm{O} + {}^{12}\mathrm{C}$ ones [14,15], although the density dependence adopted there is purely phenomenological as mentioned above and has no logical relation to the realistic three-body forces.

Considering such a situation, in the present article we propose new complex G-matrix interactions, which are applicable up to high density near twice the saturation density with the use of two-body as well as three-body NN forces and, as a first step, we apply them to proton-nucleus elastic scattering and test their validity. The application to nucleus-nucleus systems will be reported in a forthcoming article.

In Sec. II, we construct a new type of G-matrix interaction based on the first-order Brueckner theory and show some details of the folding-model calculation of the nucleon-nucleus optical potential. The results and discussion are given in Sec. III and the final section will be devoted to summary and conclusions.

II. FORMALISM

A. Derivation of complex G-matrix interaction

On the basis of the method given in Ref. [7], we derive the G-matrix interactions in symmetric nuclear matter, including a propagating nucleon with a positive energy E and a momentum $\boldsymbol{k}$. Here, the important parts in the formalism are recaptured.

Let us consider the nucleon pair of the moving nucleon with momentum $\boldsymbol{k}$ and a bound nucleon with momentum $\boldsymbol{p}$ in nuclear matter with Fermi momentum k_F. Relative and center-of-mass momenta are given as $\boldsymbol{k}_r = (\boldsymbol{k} - \boldsymbol{p})/2$ and $\boldsymbol{K}_c = \boldsymbol{k} + \boldsymbol{p}$, respectively. With a NN interaction V, the G-matrix equation giving the scattering of the pair in medium is represented as

$$G(\omega) = V + \sum_{\boldsymbol{q}_1,\boldsymbol{q}_2} V \frac{Q(\boldsymbol{q}_1,\boldsymbol{q}_2)}{\omega - e(q_1) - e(q_2) + i\varepsilon} G(\omega), \quad (1)$$

where $e(q)$ is a single-particle (s.p.) energy in an intermediate state with momentum q and $Q(\boldsymbol{q}_1,\boldsymbol{q}_2)$ is a Pauli blocking operator defined by

$$Q(\boldsymbol{q}_1,\boldsymbol{q}_2)|\boldsymbol{q}_1,\boldsymbol{q}_2\rangle = \begin{cases} |\boldsymbol{q}_1,\boldsymbol{q}_2\rangle & \text{if } q_1, q_2 > k_F, \\ 0 & \text{otherwise.} \end{cases} \quad (2)$$

The starting energy ω is given as a sum of the energy $E(k)$ of the propagating nucleon and a single-particle energy $e(p) = \frac{\hbar^2}{2m}p^2 + U[p, e(p)]$ of a bound nucleon.

The G-matrix calculations are performed with the so-called continuous choice for intermediate nucleon spectra, playing an essential role especially for imaginary parts of G matrices. This choice means that single-particle energies

$$e(q) = \frac{\hbar^2}{2m}q^2 + U[q, e(q)] \quad (3)$$

are calculated self-consistently not only for bound states ($q \leqslant k_F$) but also for intermediate states ($q > k_F$). The scattering boundary condition $i\varepsilon$ in the dominator leads to complex G matrices, summation of which gives the complex single-particle potential $U[q, e(q)]$. The plausible way is to use this self-consistent complex potential in G-matrix equation (1). Avoiding numerical complexities in such a procedure, however, we use here its real part $U_R(q) = \mathrm{Re}\, U[q, e(q)]$ in the self-consistency process as well as various works in the past [1–9]. Then, the energy E and the momentum k of the propagating nucleon are determined by the dispersion relation $E(k) = \frac{\hbar^2}{2m}k^2 + \mathrm{Re}\, U[k, E(k)]$. If we use the complex single-particle spectra in the intermediate states, the obtained imaginary parts in the G matrices may be changed significantly from those in the present treatment. In our analyses for p-nucleus scattering, however, the imaginary parts in the folding potentials derived from G matrices are adapted phenomenologically to reproduce the observed total reaction cross sections. Therefore, our important conclusions in the present work are considered to be rather independent from theoretical ambiguities of the calculated imaginary parts.

The G-matrix equation (1) is represented in each (T, S, L, J) state of a pair. L, S, and J are angular momenta of relative-orbital, spin, and total states, respectively, and T denotes isospin. The NN interaction, including tensor components, is written as $V_{LL'}^{TSJ}(r)$. The equation in coordinate

space is then expressed as

$$u^{TSJ}_{LL'}(r;q) = j_L(qr)\,\delta_{LL'} + 4\pi \sum_{L''} \times \int_0^\infty r'^2 dr'\, F_L(r,r';q)\, V^{TSJ}_{L'L''}(r')\, u^{TSJ}_{LL''}(r';q),$$

$$F_L(r,r';q) = \frac{1}{2\pi^2}\int_0^\infty q'^2 dq' \times \frac{\bar{Q}(q',\bar{K}_c;k_F) j_L(q'r) j_L(q'r')}{\omega - \left[\frac{\hbar^2}{m}q'^2 + \frac{\hbar^2}{4m}\bar{K}_c^2 + U_R(\bar{q}'_+) + U_R(\bar{q}'_-)\right]} \tag{4}$$

where $j_L(qr)$ is a spherical Bessel function for incident momentum q and $u^{TSJ}_{LL'}(r;q)$ is the corresponding scattering wave function. $\bar{Q}$, $\bar{K}_c$, and $\bar{q}'_\pm$ are the angle-averaged expressions for the Pauli operator Q, center-of-mass momentum $\boldsymbol{K}_c$, and $|\boldsymbol{q}' \pm \frac{1}{2}\boldsymbol{K}_c|$, respectively. Then, the G-matrix elements and the single-particle potentials are given as follows:

$$\langle q|G^{TSJ}_{LL'}|q\rangle = 4\pi \sum_{L''}\int_0^\infty r^2 dr j_L(qr) \times V^{TSJ}_{LL''}(r)\, u^{TSJ}_{LL''}(r;q), \tag{5}$$

$$U[k,E(k);k_F] = \frac{1}{2\pi^2}\int_0^\infty q^2 dq Z(q;k,k_F) \times \sum_{TSJT}\frac{1}{2}(2J+1)(2T+1)\langle q|G^{TSJ}_{LL}|q\rangle, \tag{6}$$

with

$$Z(q;k,k_F) = \frac{1}{kq}\left[k_F^2 - (k-2q)^2\right]. \tag{7}$$

As an important higher effect, we take into account the contribution from the so-called starting-energy rearrangement diagram. Then, the single-particle potential is given as

$$\tilde{U}[k,E(k);k_F] = (1-\bar{\mathcal{K}})\,U[k,E(k);k_F]. \tag{8}$$

Here, $\bar{\mathcal{K}}$ is the averaged value of the correlation probability $\mathcal{K}(p)$, p being a bound-state momentum. The expression for $\mathcal{K}(p)$ is obtained, if $G(\omega)$ included in that for $U[p,e(p)]$ is replaced by $-\frac{\partial G(\omega)}{\partial\omega}$.

The G-matrix interaction represented as a local form in the coordinate space can be given as follows [2]:

$$G^{TSJ}_{LL'}[r;k_F,E(k)] = \frac{\int_0^\infty q^2 dq Z(q;k,k_F) j_{L'}(qr)\sum_{L''} V^{TSJ}_{L'L''}(r) u^{TSJ}_{LL''}(r;q)}{\int_0^\infty q^2 dq Z(q;k,k_F) j_{L'}(qr) j_L(qr)}, \tag{9}$$

where the q dependence in the G matrix (5) is averaged over to reproduce the single-particle potential (6) in the first-order perturbation. The apparent k dependence in the right side is attributed to the E dependence through the dispersion relation. The obtained interaction $G^{TSJ}_{LL'}(r)$ is simulated by a linear combination of Gaussian functions with different range parameters separately for real and imaginary parts. Although this Gaussian fitting is more exact for a larger number of range parameters, we adopt a three-range representation for simplicity. Further sophistication for the fitting is not necessary for our purpose: We confirmed that the four-range Gaussian fitting for our G matrices does not lead to any meaningful change of p-nucleus scattering observables calculated in this work. In the three-range Gaussian parametrization, the outer two ranges are determined by fitting the radial form of $G^{TSJ}_{LL}(r)$ in long- and intermediate-range regions, and the innermost parts are fixed so as to reproduce the $(TSLJ)$ state contributions to the single-particle potential U. The J-independent central parts $G^{TS}_{LL}(r)$ are obtained by averaging $G^{TSJ}_{LL}(r)$ with the statistical weight $(2J+1)$. The LS components also are given by the adequate linear combinations of G^{TSJ}_{LL} on J. The L dependence of $G^{TS}_{LL}(r)$ is further averaged for each parity state with the statistical weight $(2L+1)\int_0^\infty q^2 dq Z(q;k,k_F) j_L(qr) j_L(qr)$ [2]. The obtained potential $G^{TS}_{\pm}(r)$ is refitted in a three-range Gaussian form, $\pm$ denoting even and odd parities.

As for the NN interaction model, we adopt the extended soft core (ESC) model proposed by T. A. Rijken [16,17]. Though many NN interaction models have been proposed so far, the recent models reproduce the experimental phase shifts equally well. The G-matrix interactions derived from these models as well as ESC are considered to give rise to similar results for nucleon-nucleus scattering observables. A reason for adopting ESC here is in the nuclear saturation problem. As is well known, the empirical saturation point cannot be reproduced by the lowest-order Brueckner theory (the G-matrix approximation), even if one use any two-body NN interaction model. This deficiency can be corrected clearly by introducing the three-body force (TBF) composed of the three-body attraction (TBA) and the three-body repulsion (TBR) [18–20]. The TBA is typically due to two-pion exchange with excitation of an intermediate Δ resonance, that is the Fujita-Miyazawa diagram, which gives an important contribution at low densities. In this work, we derive the effective two-body interaction from the TBA, which is added on our G-matrix interaction, according to the formalism in Ref. [21]. In our calculations, the pionic form-factor mass is taken as 420 MeV rather arbitrarily, and the NN correlation effect for the TBA is not taken into account. Then, the TBA contribution at normal-density matter is -2.3 MeV. Though out treatment for the TBA is not so rigorous quantitatively, the TBA contribution does not bring about meaningful effects on proton-nucleus scattering observables, as shown later.

The role of the TBR is far more important than that of the TBA in our present analyses. The TBR contribution becomes more and more remarkable as the density becomes higher, which plays a decisive role for the saturation curve. It is well known that such a TBR effect is indispensable to obtain the stiff equation-of-state of neutron-star matter assuring the observed maximum mass of neutron stars. However, the origin of the TBR is not necessarily established. In the ESC approach, the TBR-like effects are represented rather phenomenologically as the density-dependent two-body interactions induced by changing the vector-meson masses M_V in nuclear matter according to $M_V(\rho) = M_V \exp(-\alpha_V \rho)$ with the parameter α_V. As mentioned in Ref. [17], this TBR-like contribution introduced in ESC is found to be very similar to that of the

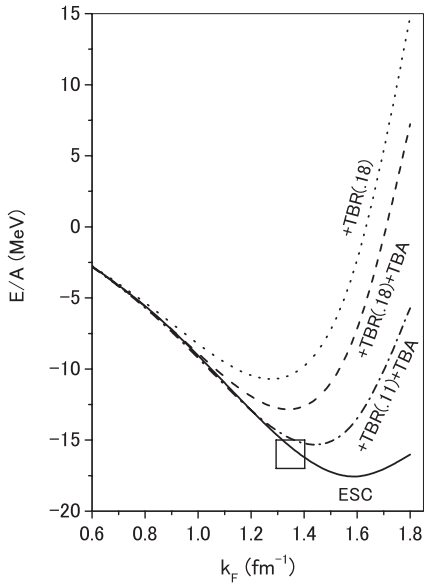

FIG. 1. Saturation curves for the four types of G-matrix interactions. See text for the meaning of four kinds of curves.

phenomenological TBR in Ref. [18] given as the density-dependent two-body repulsion.

Figure 1 shows the saturation curves obtained from the G-matrix calculations with the continuous choice. The solid curve is obtained from the two-body interaction ESC only, and the dotted one includes the TBR contribution with $\alpha_V = 0.18$. The dashed (dot-dashed) curve includes both the contributions from the TBA and the TBR with $\alpha_V = 0.18$ ($\alpha_V = 0.11$). The box represents the area in which saturation occurs empirically. The minimum point of the solid curve is far from this box, and those of the dashed and dotted ones come close to the box owing to the TBF contributions. It should be noted that the rapid-rising behaviors of the dashed and dotted curves at the high-density region are caused by the TBR contributions. The TBA contributions are seen in the change from the dotted curve to the dashed one, which are found to be moderate as a function of density. This means that the TBA is not so relevant to forms of nucleon-nucleus folding potentials differently from the TBR. The nuclear incompressibility K is an important quantity to characterize the saturation curve. The obtained values of K are 84, 173, and 260 MeV, respectively, in the cases of solid, dot-dashed, and dashed curves. The strong TBR ($\alpha_V = 0.18$) contribution in the last case brings about the large values of $K = 260$ MeV, which is consistent with the constraint by the observed neutron-star mass and the production data of hard photons in high energy central heavy-ion collisions [12].

Our Gaussian-parametrized G-matrix interaction is named CEG07. In this work, we propose the three types of CEG interactions: CEG07a, CEG07b, and CEG07c. CEG07a is derived from ESC only, and CEG07b is derived from ESC + TBA + TBR ($\alpha_V = 0.18$). In the case of CEG07c derived from ESC + TBA + TBR ($\alpha_V = 0.11$), also the ω-rearrangement effect is taken into account, which works repulsively. The repulsive contributions in the cases of CEG07b and CEG07c are due to the stronger TBR and the moderate TBR added by the ω-rearrangement effect, respectively. The calculated values of $\bar{\mathcal{K}}$ in Eq. (8) are parametrized as a function of k_F:

$$\bar{\mathcal{K}} = 0.04113 + 0.05881\,k_F + 0.02179\,k_F^2. \tag{10}$$

We tested also the version derived from ESC+TBR ($\alpha_V = 0.18$) without the TBA contribution. Then, it was found that all the results for this version are very similar to those for CEG07b: The role of the TBA is not essential for the quantities discussed in this article.

B. Folding model potential

Now, we apply the new types of G-matrix interactions, CEG07a–CEG07c, together with the original version of the CEG interaction, which we refer to CEG86 hereafter, in calculating the proton-nucleus optical potential based on the folding model and examine them by comparing with experimental data on the cross section and analyzing power of proton-nucleus elastic scattering.

In general, proton-nucleus optical model potential (OMP) will be written as

$$U = V_N + iW_N + (V_{\rm LS} + iW_{\rm LS})\boldsymbol{\ell}\cdot\boldsymbol{\sigma} + V_{\rm Coul}, \tag{11}$$

where V_N, W_N denote the real and imaginary components of the central part of OMP, whereas $V_{\rm LS}$, $W_{\rm LS}$ are the real and imaginary ones of the spin-orbit (LS) part and $V_{\rm Coul}$ is the Coulomb potential.

In this article, we construct the proton-nucleus OMP based on the folding model using the three-types of new complex G-matrix NN interactions discussed in the previous section. The central and LS parts of the NN interaction give rise to the central and LS parts of the proton-nucleus folding-model potential (FMP), respectively.

For the central part, we calculated FMP on the same method described in Ref. [7]. The proton-nucleus FMP at an incident energy E_p is given by

$$\begin{aligned} &V_N(\boldsymbol{r}_1; E_p) + iW_N(\boldsymbol{r}_1; E_p) \\ &= \int \left\{\rho_p(\boldsymbol{r}_2) T_{pp}^{\rm D}\left[\boldsymbol{s}; k_F^{(pp)}, E_p\right]\right. \\ &\quad \left. + \rho_n(\boldsymbol{r}_2) T_{pn}^{\rm D}\left[\boldsymbol{s}; k_F^{(pn)}, E_p\right]\right\} d\boldsymbol{r}_2 \\ &\quad + \int \left\{\rho_p(\boldsymbol{r}_1, \boldsymbol{r}_2') T_{pp}^{\rm EX}\left[\boldsymbol{s}; k_F^{(pp)}, E_p\right]\right. \\ &\quad \left. + \rho_n(\boldsymbol{r}_1, \boldsymbol{r}_2') T_{pn}^{\rm EX}\left[\boldsymbol{s}; k_F^{(pn)}, E_p\right]\right\} j_0(ks) d\boldsymbol{r}_2' \end{aligned} \tag{12}$$

where ρ_p and ρ_n are the proton and neutron densities, respectively, of the target nucleus. The coordinate $\boldsymbol{s}$ is the relative vector between the incident proton and a nucleon in the target nucleus that interacts with the incident proton, $\boldsymbol{s} = \boldsymbol{r}_2 - \boldsymbol{r}_1$. The direct (D) and exchange (EX) parts of the proton-proton (pp) and proton-neutron (pn) G-matrix interaction are written as

$$T_{pp}^{\rm D,EX} = \tfrac{1}{4}(t^{01} \pm 3t^{11}), \tag{13}$$

$$T_{pn}^{\rm D,EX} = \tfrac{1}{8}(\pm t^{00} + t^{01} + 3t^{10} \pm 3t^{11}), \tag{14}$$

in terms of $t^{\rm ST}$, the spin-isospin component ($S = 0$ or 1 and $T = 0$ or 1) of the G-matrix interaction. Here, the upper

and lower part of the double-sign symbols correspond to the direct (D) and exchange (EX) parts, respectively. The local momentum k which appears in Eq. (11) is defined as

$$k = \left\{ \frac{2\mu}{\hbar^2}[E_{\rm c.m.} - V_N(\boldsymbol{r}_1; E) - V_{\rm Coul}(\boldsymbol{r}_1)] \right\}^{1/2}, \quad (15)$$

where μ is the reduced mass of the proton-nucleus system. For finite nuclei with $N \neq Z$, the proton Fermi momentum $k_F^{(p)} = (3\pi^2\rho_p)^{1/3}$ is in general different from the neutron one $k_F^{(n)} = (3\pi^2\rho_n)^{1/3}$. Here, the local densities ρ_p and ρ_n are evaluated at a middle point of the interacting nucleons, $(\boldsymbol{r}_1 + \boldsymbol{r}_2)/2$, throughout the present article. Therefore, when we evaluate the density dependence of the G-matrix interaction in Eq. (12), we use different Fermi momenta for the pp interaction $T_{pp}^{\rm D,EX}[\boldsymbol{s}; k_F^{pp}, E_p]$ and the pn one $T_{pn}^{\rm D,EX}[\boldsymbol{s}; k_F^{pn}, E_p]$ following the original GEG86 prescription [8] as

$$k_F^{(pp)} = k_F^{(p)}, \quad (16)$$

$$k_F^{(pn)} = \tfrac{1}{2}\left[k_F^{(p)} + k_F^{(n)}\right]. \quad (17)$$

The density matrix $\rho(\boldsymbol{r}, \boldsymbol{r}')$ is approximated in the same manner as in Ref. [22];

$$\rho_p(\boldsymbol{r}, \boldsymbol{r}') = \frac{3}{k_{F,pp}^{\rm eff} \cdot s} j_1\left(k_{F,pp}^{\rm eff} \cdot s\right) \rho_p\left(\frac{\boldsymbol{r} + \boldsymbol{r}'}{2}\right), \quad (18)$$

$$\rho_n(\boldsymbol{r}, \boldsymbol{r}') = \frac{3}{k_{F,pn}^{\rm eff} \cdot s} j_1\left(k_{F,pn}^{\rm eff} \cdot s\right) \rho_n\left(\frac{\boldsymbol{r} + \boldsymbol{r}'}{2}\right), \quad (19)$$

where $k_{F,pp}^{\rm eff}$ and $k_{F,pn}^{\rm eff}$ are the effective Fermi momenta [23] defined by

$$k_{F,pp}^{\rm eff} = \left\{ \left(3\pi^2\rho_p\right)^{2/3} + \frac{5C_s\left[\nabla\rho_p^2\right]}{3\rho_p^2} + \frac{5\nabla^2\rho_p}{36\rho_p} \right\}^{1/2}, \quad (20)$$

$$k_{F,pn}^{\rm eff} = \frac{1}{2}\left(\left\{ (3\pi^2\rho_p)^{2/3} + \frac{5C_s\left[\nabla\rho_p^2\right]}{3\rho_p^2} + \frac{5\nabla^2\rho_p}{36\rho_p} \right\}^{1/2} + \left\{ (3\pi^2\rho_n)^{2/3} + \frac{5C_s\left[\nabla\rho_n^2\right]}{3\rho_n^2} + \frac{5\nabla^2\rho_n}{36\rho_n} \right\}^{1/2} \right), \quad (21)$$

where we adopt $C_s = 1/4$ following Ref. [24]. The different value of $C_s = 1/16$ was also suggested [24]. So, we have tested the latter value but we have found that no significant difference from the case with $C_s = 1/4$ is observed in the present proton-nucleus scattering.

When we calculate the imaginary part of FMP, the imaginary part of G-matrix interaction is multiplied by the ratio of the k mass to the bare mass following the standard prescription of Ref. [8,25];

$$\mathrm{Im}\, T^{\rm D,EX} \to \frac{m_k}{m} \mathrm{Im}\, T^{\rm D,EX}, \quad (22)$$

where m is the bare mass of a nucleon and m_k is the k mass defined in Ref. [5]. This leads to a reduction of the imaginary part of folding potential at short distances by about 20–30% at low energies and about 10% at high energies. However, the effect of k mass is found to show only a negligible effect on the cross sections and analyzing powers of the proton-nucleus elastic scattering discussed in the present article.

The proton-nucleus spin-orbit (LS) potential is also calculated by folding the LS part of the G-matrix interaction with the nucleon density of the target nucleus, which is also composed of the direct and exchange parts;

$$U_{\rm LS}(\boldsymbol{r}_1; E_p) = U_{\rm LS}^{\rm D}(\boldsymbol{r}_1; E_p) + U_{\rm LS}^{\rm EX}(\boldsymbol{r}_1; E_p). \quad (23)$$

The direct part of the folding-model LS potential is calculated in the same way as in Ref. [4];

$$U_{\rm LS}^{\rm D}(\boldsymbol{r}_1; E_{\rm p}) = \frac{1}{4r_1^2} \int \boldsymbol{r}_1 \cdot (\boldsymbol{r}_1 - \boldsymbol{r}_2) \left\{ \rho_{\rm p}(\boldsymbol{r}_2) T_{{\rm LS},pp}^{\rm D}\left[\boldsymbol{s}; k_F^{(pp)}, E_p\right] + \rho_n(\boldsymbol{r}_2) T_{{\rm LS},pn}^{\rm D}\left[\boldsymbol{s}; k_F^{(pn)}, E_p\right] \right\} d\boldsymbol{r}_2. \quad (24)$$

The exchange part is also divided into contributions from protons and neutrons in the target nucleus as

$$U_{\rm LS}^{\rm EX}(\boldsymbol{r}_1; E_p) = U_{{\rm LS},p}^{\rm EX}(\boldsymbol{r}_1; E_p) + U_{{\rm LS},n}^{\rm EX}(\boldsymbol{r}_1; E_p). \quad (25)$$

In evaluating the exchange part, we use the modified LS folding method described in Ref. [4], except that, in our calculation, Eq. (15) of Ref. [4] is replaced by the following corrected expression,

$$\begin{aligned} U_{{\rm LS},\alpha}^{\rm EX}(\boldsymbol{r}_1; E_p)\boldsymbol{\ell}\cdot\boldsymbol{\sigma} &= -\frac{i\hbar}{4} \int d\boldsymbol{r}_2 T_{{\rm LS},p\alpha}^{\rm EX}\left[s; k_F^{(p\alpha)}, E_p\right](\boldsymbol{s}\times\boldsymbol{\nabla}_1)\cdot\boldsymbol{\sigma}_1 \\ &\quad \times \rho_\alpha\left(\left|\boldsymbol{r}_1 + \frac{1}{2}\boldsymbol{s}\right|\right) \frac{3}{k_F^{(p\alpha)}\cdot s} j_1\left[k_F^{(p\alpha)}\cdot s\right] e^{i\boldsymbol{k}\cdot\boldsymbol{s}} \\ &\quad + \frac{i\hbar}{4} \int d\boldsymbol{r}_2 T_{{\rm LS},p\alpha}^{\rm EX}\left[s; k_F^{(p\alpha)}, E_p\right] \rho_\alpha\left(\left|\boldsymbol{r}_1 + \frac{1}{2}\boldsymbol{s}\right|\right) \\ &\quad \times \frac{3}{k_F^{(p\alpha)}\cdot s} j_1\left[k_F^{(p\alpha)}\cdot s\right](\boldsymbol{s}\times\boldsymbol{\nabla}_2)\cdot\boldsymbol{\sigma}_1 e^{i\boldsymbol{k}\cdot\boldsymbol{s}}, \end{aligned} \quad (26)$$

where α represents p or n. The derivative with respect to the coordinate $\boldsymbol{s}$, $\boldsymbol{\nabla}_s$, should act also on the wave function $\phi(r_2)$, whereas in Ref. [4] $\boldsymbol{\nabla}_s\phi(r_2)$ was ignored. Equation (26) is then finally reduced, by the same method as in Ref. [4], to

$$U_{{\rm LS},\alpha}^{\rm EX}(\boldsymbol{r}_1; E_p) = \pi \int ds s^3 \left[\frac{2j_0(ks)}{r_1} \rho_1^{(\alpha)}(r_1, s) + \frac{j_1(ks)}{2k} \delta_0^{(\alpha)}(r_1, s) \right], \quad (27)$$

where

$$\begin{aligned} \delta_0^{(\alpha)}(r_1, s) &= \frac{1}{2}\int_{-1}^{+1} d\omega \frac{T_{LS,p\alpha}^{\rm EX}\left[s; k_F^{(p\alpha)}, E_p\right]}{x} \\ &\quad \times \left\{ \frac{3}{k_{F,p\alpha}^{\rm eff}\cdot s} j_1\left(k_{F,p\alpha}^{\rm eff}\cdot s\right) \frac{d}{dx}\rho_\alpha(x)\Big|_{x=\sqrt{r_1^2+s^2/4+r_1 s\omega}} \right. \\ &\quad + s\rho_\alpha(x)\frac{d}{dx}k_{F,p\alpha}^{\rm eff}(x)\Big|_{x=\sqrt{r_1^2+s^2/4+r_1 s\omega}} \\ &\quad \left. \times \frac{d}{dy}\left[\frac{3}{y}j_1(y)\right]\Big|_{y=k_{F,p\alpha}^{\rm eff}\cdot s} \right\}, \end{aligned} \quad (28)$$

$$\rho_1^{(\alpha)}(r_1, s) = \frac{1}{2}\int_{-1}^{+1} d\omega\omega T_{\mathrm{LS},p\alpha}^{\mathrm{EX}}\left[s; k_F^{(p\alpha)}, E_p\right]\frac{3}{k_{F,p\alpha}^{\mathrm{eff}}\cdot s} \times j_1\left(k_{F,p\alpha}^{\mathrm{eff}}\cdot s\right)\rho_\alpha(y)\big|_{y=\sqrt{r_1^2+s^2/4+r_1 s\omega}}. \quad (29)$$

The LS part of the G-matrix interaction is also written as follows;

$$T_{\mathrm{LS},pp}^{\mathrm{D,EX}} = \pm t_{\mathrm{LS}}^{11}, \quad (30)$$

$$T_{\mathrm{LS},pn}^{\mathrm{D,EX}} = \tfrac{1}{2}\left(t_{\mathrm{LS}}^{10} \pm t_{\mathrm{LS}}^{11}\right). \quad (31)$$

The meaning of the above expressions is similar to that of Eq. (13) and (14).

III. RESULTS AND DISCUSSION

A. Calculated folding model potentials

We now show the calculated FMP and its application to the proton elastic scattering by various target nuclei, ^{12}C, ^{40}Ca, ^{90}Zr, and ^{208}Pb, observed at incident energies of $E_p = 65 \sim 200$ MeV. For ^{12}C, the nucleon (point) densities are taken from the 3α-RGM calculation by Kamimura [26] and for ^{40}Ca, ^{90}Zr, and ^{208}Pb we adopt the density-dependent Hartree-Fock (DDHF) calculation by Negele [27]. The DDHF calculation provides with the different density profiles for protons and neutrons. For all the target nuclei discussed here, the adopted proton density is known to well reproduce the electron-scattering experiment if it is converted to the charge density by folding the finite size of proton charge. Needless to say, it is essential to distinguish the charge-density distribution from the proton point-density distribution [the distribution of the center-of-mass (c.m.) of protons] when it is used in the folding model calculation.

First, we compare the potentials obtained by the folding of different types of G-matrix interactions. We have tested four types of interactions: CEG86 that is the original CEG-type interaction proposed in Ref. [8] and three types of new complex G-matrix interactions (CEG07a, CEG07b, and CEG07c). Figures 2 and 3 show the real and imaginary parts of the central and LS components of FMP for ^{12}C and ^{208}Pb target nuclei calculated at a proton incident energy of $E_p =$ 200 MeV. The effects due to the use of different types of G-matrix interactions are very similar for the two target nuclei, although the detail shapes and magnitudes of FMP are rather different between the two target nuclei, which is natural reflecting the different size and density distribution of the nuclei. The main characteristics of these figures are very similar for other target nuclei or different incident energies investigated here.

The effect of the TBF is clearly seen in the short- and medium-range region of the real central potential by comparing the CEG86 and CEG07a results with the GEC07b and CEG07c ones, the latter two containing the TBR and the TBA contributions, as mentioned before. It is found that the large contribution of TBF in the real central FMP is mainly due to the TBR contribution, whereas the TBA contribution is found to be small in the real central part. As for the imaginary part, the results with CEG07a and CEG07b have

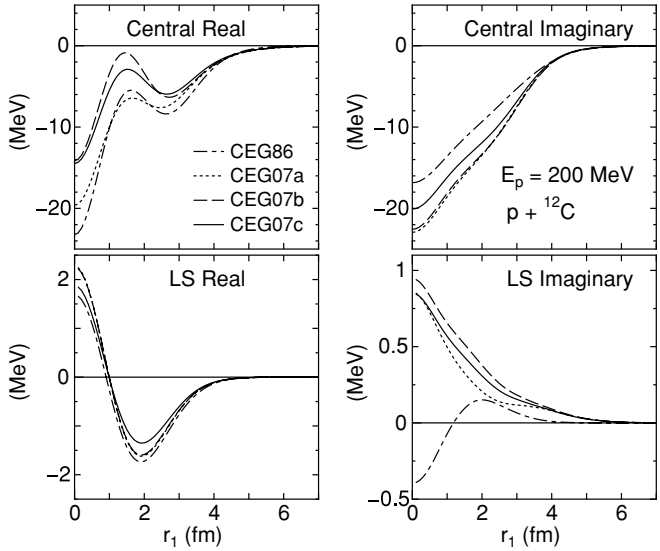

FIG. 2. The real and imaginary parts of the central and LS components of FMP obtained by four types of G-matrix interactions for the ^{12}C target evaluated at $E_p = 200$ MeV. The dot-dashed, dotted, dashed, and solid curves are the results with CEG86, CEG07a, CEG07b, and CEG07c, respectively.

a very similar shape over the whole radial range. However, this does not necessarily imply that the TBF effect on the imaginary FMP is negligible. In fact, it is found that the individual contributions of TBR and TBA to the imaginary FMP, which are not separately shown here, are rather large but they have opposite effects and cancel out, leading to an almost negligible effect as a whole in the imaginary central FMP. In fact, this balance disappears in the case of CEG07c in which a weaker TBR ($a_V = 0.11$) effect compared with the CEG07b ($a_V = 0.18$) case is included, although CEG07c also contains the ω-rearrangement effect.

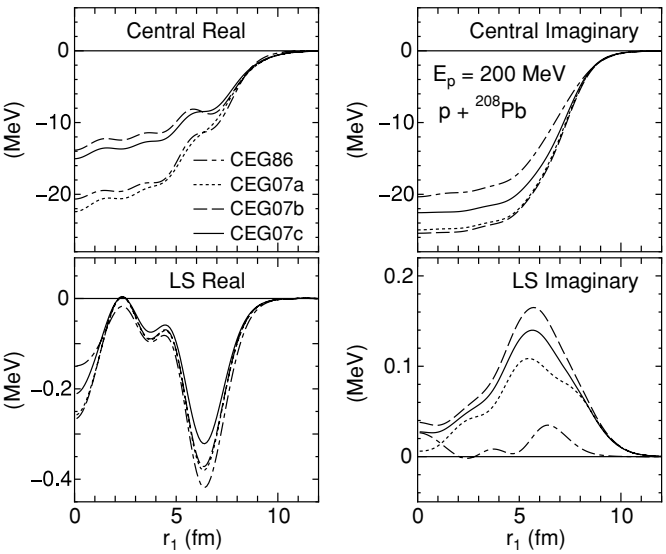

FIG. 3. The same as described in the caption to Fig. 2 but for the ^{208}Pb target.

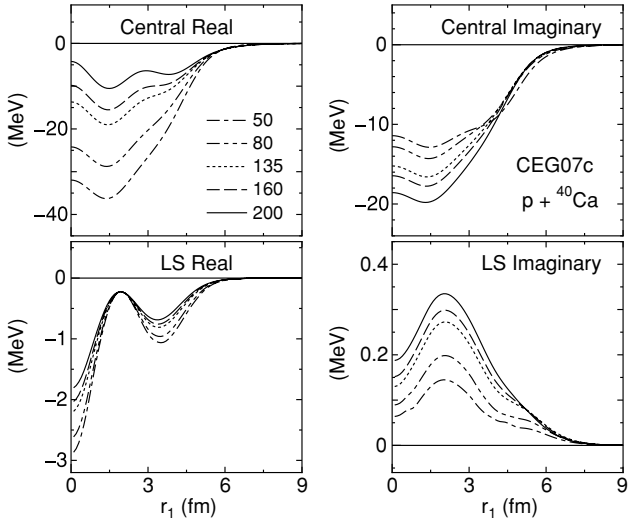

FIG. 4. The energy dependence of FMP for the ^{40}Ca target with the CEG07c interaction. The dot-dashed, double-dot-dashed, dotted, dashed, and solid curves are for the proton incident energy of $E_p =$ 50, 80, 135, 160, and 200 MeV, respectively.

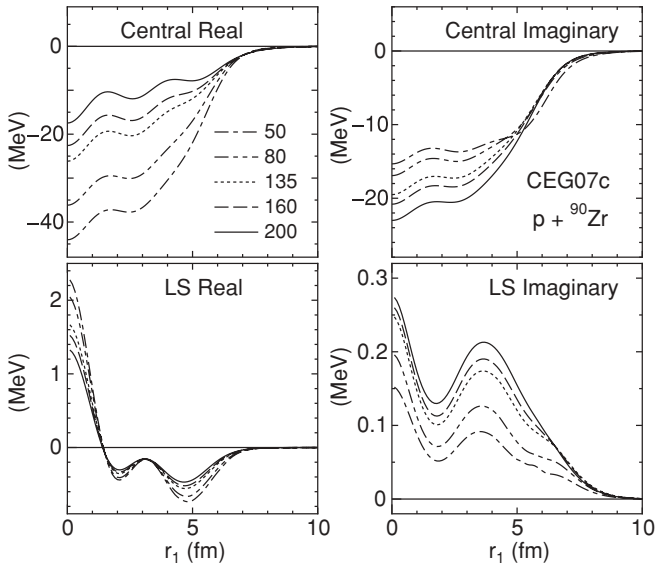

FIG. 5. The same as described in the caption to Fig. 4 but for the ^{90}Zr target.

However, in the LS part of FMP, little difference is observed among the four types of interactions, except that CEG86 gives rise to a noticeable deviation in the imaginary LS part from those with other three interactions. One should note, however, that the absolute magnitude of the imaginary LS potentials themselves are very small (note the different vertical scales) and, in fact, it is found that the deviation of the imaginary LS potential for CEG86 gives rise to no visible effect on the proton-nucleus scattering observables.

Next, we show the energy dependence of FMP in the cases of ^{40}Ca and ^{90}Zr targets, as examples. Figures 4 and 5 show the energy dependence of the real and imaginary parts of the central and LS components of FMPs calculated with the CEG07c interaction in the energy range of $E_p = 50 \sim$ 200 MeV. The strength of the real part decreases as the increase of proton incident energy both in the central and LS components, whereas the strength of the imaginary part increases with the incident energy except in the nuclear surface region, which is consistent with the tendency of empirical optical potentials as well as microscopic optical potentials with other interaction models [4,6,9].

B. Total reaction cross sections

Next, we apply these FMPs to the calculation of proton-nucleus elastic scattering as well as the reaction cross sections for ^{12}C, ^{40}Ca, ^{90}Zr, and ^{208}Pb targets in the energy range of $E_p = 65 \sim 200$ MeV. In the practical application to the analysis of experimental observables, one needs to slightly modify the present FMP. Now, we have adopted the G-matrix interaction based on the lowest-order Brueckner theory in nuclear matter and constructed the proton-nucleus optical potential in the local-density approximation (LDA), in which the non-local exchange part has also been localized approximately in a standard way [4,7,8], as shown in the previous section. This kind of approach is known to somewhat overestimate the imaginary part of optical potential [6,7] and one has to introduce a renormalization (reduction) factor to the imaginary part, which is also the case with the present FMPs. So, we introduce the renormalization factor, say $N_{\rm W}$, to the imaginary part of calculated FMP, which is taken to be common to the central and LS components, as

$$U_{\rm opt} = V_N + iN_{\rm W}W_N + (V_{\rm LS} + iN_{\rm W}W_{\rm LS})\boldsymbol{\ell}\cdot\boldsymbol{\sigma} + V_{\rm Coul}, \quad (32)$$

and we fix the factor $N_{\rm W}$ so that the renormalized FMP reproduces the experimental data of proton-nucleus total reaction cross sections.

Figure 6 shows the total reaction cross sections measured at $E_p = 50 \sim 200$ MeV for ^{12}C, ^{40}Ca, ^{90}Zr, and ^{208}Pb targets which are compared with the calculated ones with the use of FMPs based of the four types of G-matrix interactions. It should be emphasized that, for each type of G-matrix interaction, the measured reaction cross sections are well reproduced by FMP with a *single* value of N_W, irrespective of the proton incident energy E_p or target nucleus. The optimum value of N_W for each type of G-matrix interaction is summarized in Table I. These values are consistent with the different strength of the imaginary part of original FMPs shown in Figs. 2 and 3. For example, the same values for CEG07a and CEG07b are due to the almost same strength and shape of FMPs calculated with these interactions, while the largest value of N_W for CEG86 reflects the smallest strength of imaginary part of FMP obtained by this interaction.

TABLE I. Renormalization factors (N_W) for the imaginary part of the FMP needed to reproduce the total reaction cross-section data, shown in Fig. 6, with FMPs generated by different types of complex G-matrix interactions.

Interactions	CEG86	CEG07a	CEG07b	CEG07c
N_W	0.80	0.65	0.65	0.70

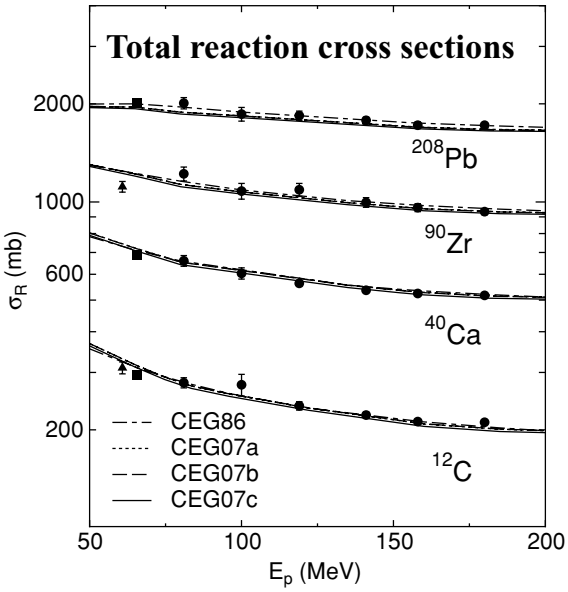

FIG. 6. Energy dependence of the total reaction cross sections for the proton-^{12}C, ^{40}Ca, ^{90}Zr, and ^{208}Pb systems. Experimental data are from Refs. [28–30]. The meaning of the curves are the same as in Fig. 2.

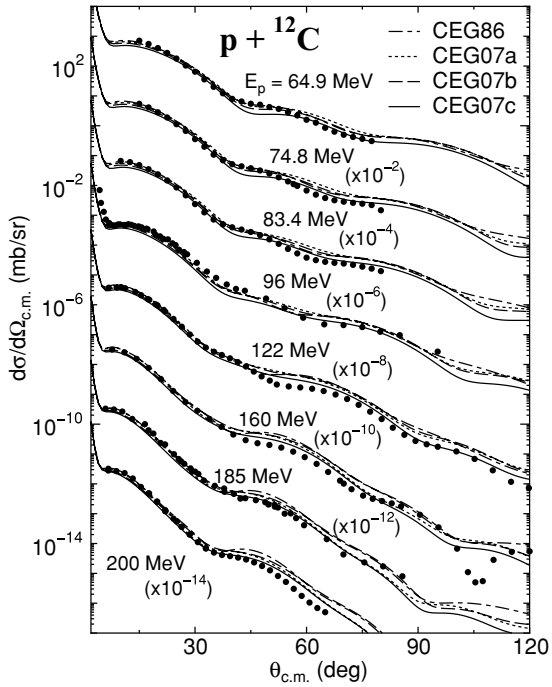

FIG. 7. Differential cross sections for proton elastic scattering by ^{12}C at $E_p = 64.9$, 74.8, 83.4, 96, 122, 160, 185, and 200 MeV, which are compared with the folding model calculations with the four types of effective interactions. The meaning of the curves are the same as in Fig. 2. Experimental data are taken from Refs. [31–35].

These results suggest that the present FMP with the fixed renormalization factor given in Table I for the imaginary part has a predicting power of total reaction cross sections for other target nuclei and/or incident energies at least within the range investigated here, $A_T = 12 \sim 208$ and $E_p = 50 \sim 200$ MeV.

C. Differential cross sections and analyzing powers

Once the renormalization factor for the imaginary part is fixed by the constraint of reproducing the reaction cross sections, no freely adjustable parameter is left in the present model in comparison with the experimental data for proton-nucleus elastic-scattering cross sections and analyzing powers. Therefore, it may become possible to judge which G-matrix interaction is the most successful in the description of proton-nucleus reactions and to estimate the role of effects included in the G-matrix interactions, such as the TBF as well as the density dependence that is closely related to the saturation property of the NN interaction in nuclear matter seen in Fig. 1.

Figure 7 shows the differential cross sections for proton elastic scattering by the ^{12}C target at $E_p = 64.9$, 74.8, 83.4, 96, 122, 160, 185, and 200 MeV. All the cross sections calculated with the four types of FMPs well reproduce the angular distributions of the experimental data up to backward angles. Although minor difference among the calculated ones as well as from the experimental data are observed in the middle and backward angular regions, it is rather difficult to judge which interaction is apparently better than others only from the comparison with the cross section data. Here, we should mention that the results with the CEG86 interaction (dot-dashed curves shown in Fig. 7) give better fits to the experimental data compared with those reported in the original article [8] where the CEG86 interaction was proposed. This is due to the correct treatment of folding procedure in the exchange part of the spin-orbit potential that was already mentioned in the previous section concerning to Eqs. (26)–(29).

Figure 8 shows the analyzing powers for proton elastic scattering by ^{12}C target at $E_p = 64.9$, 74.8, 83.4, 122, 160, 185, and 200 MeV. For the lowest three energies, no significant difference is observed among the calculated results with the four types of interactions as well as the experimental data, except for the most backward angles. For energies over 100 MeV, however, a clear difference is observed at forward angles, say $\theta_{\text{c.m.}} = 10 \sim 50^\circ$. Especially for $E_p = 122$ and 160 MeV, the results with CEG07b and CEG07c that include the TBF effect show apparently better agreement with the experimental data in this angular range than those with the CEG86 and CEG07a. This result is a clear indication of the important role of TBF in proton elastic scattering.

It should, however, be noted that the large effect of TBF on the analyzing power is not due to the change of the LS part of folding potential with the inclusion of TBF but mainly due to the change of the real-central component of the folding potential, the strength of which is most strongly affected by the inclusion of TBF, particularly the TBR contribution as already discussed concerning to the results shown in Fig. 2. In fact, a "modified CEG07b" potential in which only the real-central component is artificially replaced by that obtained by the CEG07a interaction produces the analyzing powers that are very close to the CEG07a results (the dotted curves in Fig. 8). One should note that the analyzing power is composed

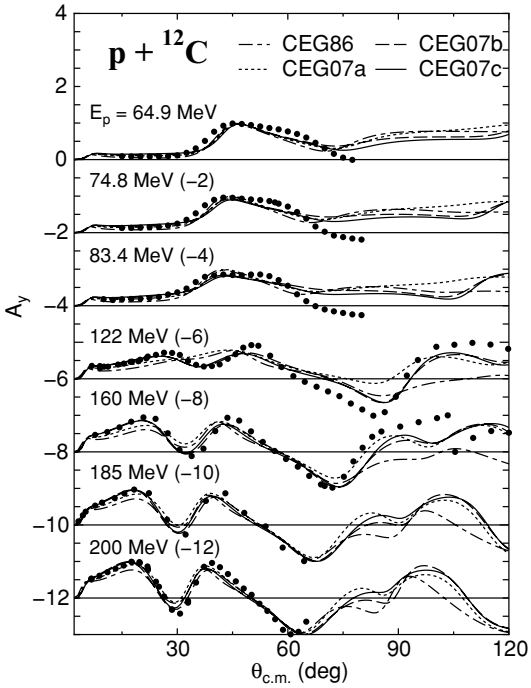

FIG. 8. Analyzing powers for proton elastic scattering by ^{12}C at $E_p = 64.9, 74.8, 83.4, 122, 160, 185$, and 200 MeV, which are compared with the folding model calculations with the four types of effective interactions. The meaning of the curves are the same as in Fig. 2. Experimental data are taken from Refs. [31,33–35].

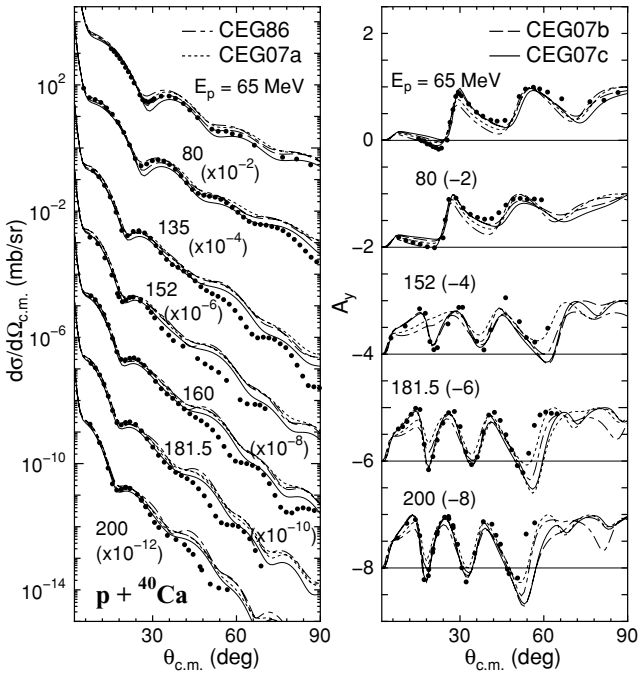

FIG. 9. The same as described in the captions to Figs. 7 and 8 but for the ^{40}Ca target at $E_p = 65, 80, 135, 152, 160, 181.5$, and 200 MeV. Experimental data are taken from Refs. [36–40].

of the product of vector amplitude that is mainly governed by the LS potential and the scalar amplitude that is mainly governed by the central potential and, in the present case, the large change of the real-central component of folding potential with the inclusion of TBF is the main source of the drastic improvement of the analyzing power at forward angles.

Similar analyses have been made for the scattering by other target nuclei. Figure 9 shows the cross sections and the analyzing powers of the elastic scattering by ^{40}Ca at $E_p = 65 \sim 200$ MeV. As in the case of ^{12}C target, no essential difference is observed in cross section calculated with the use of different effective interactions and all the calculations well reproduce the measured cross sections except those at large angles for the scattering at $E_p > 100$ MeV. It is noticed that the results with the CEG07c interaction, which contains the effect of ω-rearrangement term, show a slight but systematic deviation from those with other three interactions around backward angles.

However, a very clear difference is observed in the calculated analyzing powers at small angles ($\theta_{\text{c.m.}} < 30^\circ$), especially in the cases of $E_p = 152$ and 181.5 MeV, where CEG86 and CEG07a with no TBF included completely fail to reproduce the experimental data, whereas CEG07b and CEG07c with TBF give perfect fits to the data. Again, the clear effect of TBF (mainly TBR effect) on the analyzing power originates from the large effect of TBF on the real-central component of the folding potential, not on the LS component, as in the case of the ^{12}C target.

Figures 10 and 11 show the similar results for heavier targets, ^{90}Zr and ^{208}Pb, in the similar range of proton incident energies. Overall good agreements with the data are obtained by all the interaction models. In a closer look at the detail

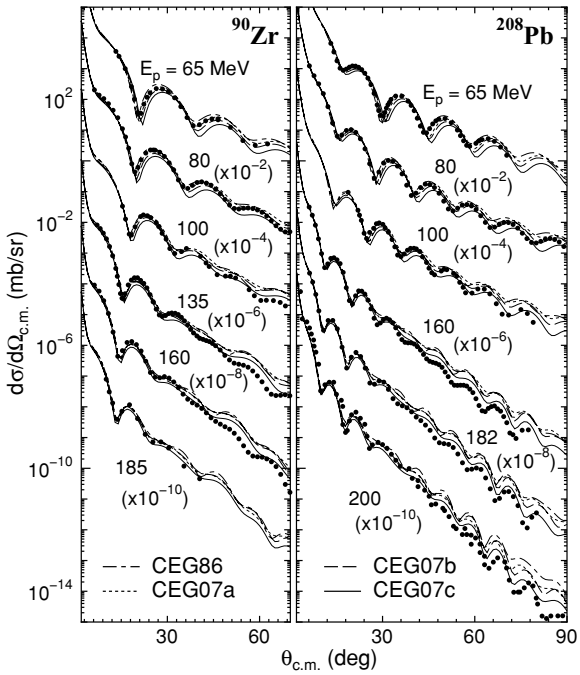

FIG. 10. The same as Fig. 7 but for cross sections on the ^{90}Zr target at $E_p = 65, 80, 100, 135, 160$, and 185 MeV and the ^{208}Pb target at $E_p = 65, 80, 100, 155, 160, 182$, and 200 MeV. Experimental data are taken from Refs. [36,38,41–43].

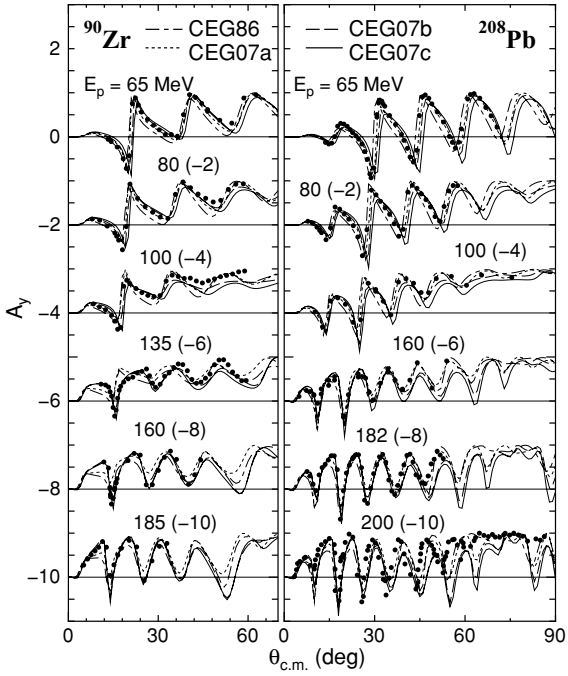

FIG. 11. The same as described in the caption to Fig. 10 but for analyzing powers. Experimental data are taken from Refs. [36,39,42,43].

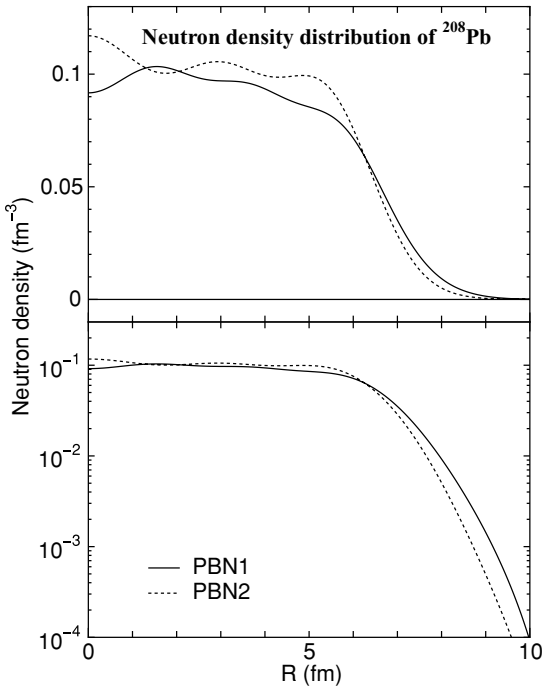

FIG. 12. Comparison of the two types of neutron densities of ^{208}Pb in the linear scale (upper panel) and in the logarithmic scale (lower panel). The solid curves (labeled as PBN1) show the neutron density obtained by the DDHF calculation [27] and the dotted curves (labeled PBN2) are the neutron density assumed to have the same profile as the proton density obtained by the DDHF calculation.

comparison, the CEG07c interaction gives a better fit to the cross-section data at middle and large angles at higher energies, whereas at lower energies the calculated cross sections slightly shift to backward angles compared with those calculated with other three interactions as well as with the experimental data. This kind of tendency has already started to appear in the case of ^{40}Ca target (Fig. 9) and seems to prominent as the target mass number increases. The reason for the angular shift of the CEG07c interaction for low-energy scattering by heavy targets is not clear now.

Again, a clear effect of TBF is seen at forward angles of analyzing powers for higher-energy scattering, especially at $E_p = 135$ and 160 MeV, in the case of the ^{90}Zr target. For the ^{208}Pb target, however, no clear effect of TBF is observed even in the analyzing powers, although CEG07b and CEG07c still give better agreements with the experimental data in the forward angle region. In the case of the ^{208}Pb target, the strong Coulomb potential may conceal the effect of TBF in nuclear folding potential that most strongly appears in the inner part of real-central component of folding potential as shown in Figs. 2 and 3.

D. Sensitivity to the neutron density distribution

In general, it is rather difficult to directly probe the neutron density distributions in nuclei compared with the proton ones that can be studied by the electromagnetic probes such as electron scattering and energy shifts of muonic atoms. The folding-model analysis of the proton elastic scattering is one of the possible probe to survey the neutron density distributions. We here examine how the present FMC is sensitive to the choice of neutron density distribution and demonstrate it in the case of ^{208}Pb target with the use of the CEG07c interaction. In this test calculation, we use two types of neutron densities. One is the neutron density obtained by the density-dependent Hartree-Fock (DDHF) calculation by Negele [27], which we have already used in the calculations shown in Figs. 10 and 11, and the other is a simple and often used prescription that the neutron density distribution is assumed to be the same as the proton one, namely the neutron density being assumed to be proportional to the proton one as $\rho_n = (N/Z)\rho_p$. We refer to the former as PBN1 and to the latter as PBN2. In both calculations, we use the same proton density obtained by the DDHF calculation [27] which reproduces the electron-scattering experiment as already mentioned. The two kinds of neutron densities are compared in Fig. 12 both in the linear and logarithmic scales. The two density profiles have rather different shapes in the middle- and short-range region and they also have different surface diffuseness, reflecting the difference between the proton and neutron density profiles predicted by the DDHF calculation. In addition, the root-mean-square (rms) radius of PBN2 is 5.37 fm that is smaller than that of PBN1 (5.58 fm) by 0.21 fm.

The difference of neutron densities clearly appears in the calculated cross sections and analyzing powers of the proton elastic scattering that are shown in Fig. 13 in the case of $E_p = 182$ MeV. The angular distribution obtained with PBN2 slightly shifts toward backward angles, which is mainly due to the smaller rms radius as well as the

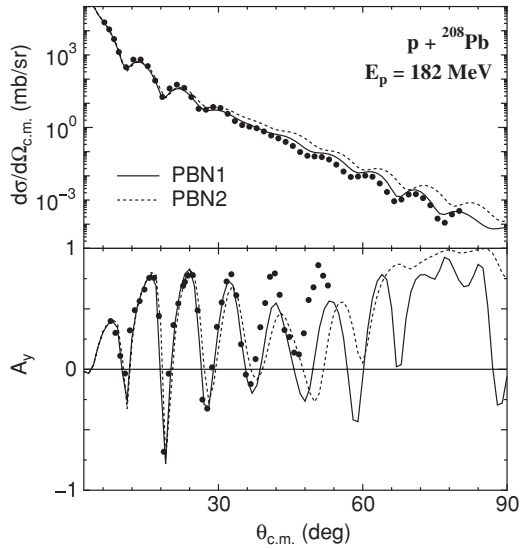

FIG. 13. Comparison of the calculated cross-section and analyzing power of proton elastic scattering at $E_p = 182$ MeV by ^{208}Pb with the use of PBN1 and PBN2 neutron densities together with the CEG07c interaction.

smaller surface diffuseness, and it is clear that the result with PBN1 gives better agreement with the experimental data. This result demonstrates the importance of using a more realistic neutron density in the folding-model analysis of proton scattering. In other words, the proton elastic scattering is very sensitive to the detailed shape of neutron density distribution in the target nucleus and one could extract detailed information about the neutron density distribution in nuclei from a precise comparison of the folding-model calculation with the experimental data of proton elastic scattering. This is of particular importance when the folding model is applied to probe unknown neutron density as well as proton density distributions in proton-rich/neutron-rich unstable nuclei.

IV. SUMMARY AND CONCLUSIONS

In this article, we have proposed three kinds of new complex G-matrix interactions, CEG07a, CEG07b, and CEG07c, the latter two of which include the effect of TBF to make the saturation curve in nuclear matter more realistic in the high-density region. The important role is played by the TBR, which works more and more repulsively in the higher-density region. This effect is known to be indispensable for a stiffening of the EOS in neutron-star matter, assuring the observed maximum mass of neutron stars. When the G-matrix interactions are applied to the double-folding-model calculation of nucleus-nucleus optical potentials, the density dependence of G-matrices at densities higher than the saturation density is critically important and the TBR effects are expected to appear more dramatically. Such a situation will be investigated in our future works.

We then apply the new types of complex G-matrix interactions to the calculation of proton-nucleus optical potentials within a framework of FMP in LDA for the cases of ^{12}C, ^{40}Ca, ^{90}Zr, and ^{208}Pb target nuclei at proton incident energies of $E_p = 65 \sim 200$ MeV and compare them with the results obtained by the use of original version of CEG-type interaction (which we call CEG86) [8]. The effect of TBF is clearly seen in the real-central component of the folding potential, the strength of which is largely reduced by the TBF effect in the middle- and short-range region of the potential, whereas the effect does not strongly affect the LS part of the folding potential. Among the TBF effect, the repulsive component of TBF (the TBR component) is found to dominate the attractive one (the TBA one). The ω-rearrangement effect included in CEG07c slightly reduces the strength of imaginary part of the central potential. These trends are common to all the target nuclei as well as to all the proton incident energies investigated here.

We then calculate the proton-nucleus reactions observables, namely the total reaction cross sections as well as the differential cross sections and analyzing powers of the elastic scattering, and compare them with the experimental data for the ^{12}C, ^{40}Ca, ^{90}Zr, and ^{208}Pb target nuclei observed at $E_p = 65 \sim 200$ MeV. To compare with the experimental data, we first introduce a renormalization factor N_W for the imaginary part of FMP and the N_W value for each G-matrix interaction is determined to reproduce the observed total reaction cross section. It is found that a single N_W value for each G-matrix interaction gives a reasonable fit to the reaction cross-section data for all the target nuclei and incident energies investigated here. Therefore, when we calculate the elastic-scattering cross sections and analyzing powers, we use the fixed value of N_W listed in Table I for each G-matrix interaction. Namely once we fix the N_W value from the reaction cross sections, there exists no adjustable parameter in the calculation of elastic-scattering observables.

From the comparison with the experimental data for elastic scattering, FMPs calculated with CEG07b and CEG07c are apparently superior to those with CEG07a and CEG86, indicating the important role of the TBF that is included in the former two interactions. The TBF effect is clearly seen, especially in the drastic improvement of the fit to the analyzing power data at forward angles, which is, however, due to the TBF effect on the real-central component of FMP, not on the LS component as discussed in detail.

We have also tested the sensitivity of FMP and proton-nucleus elastic-scattering observables to the choice of neutron density distribution in the target nucleus in the case of ^{208}Pb target and we have shown an importance of using a realistic neutron density profile that may be rather different from the proton one for heavy targets as well as for proton-rich/neutron-rich unstable nuclei.

As mentioned in the Introduction, our final goal is to construct a realistic as well as reliable microscopic model for predicting the nucleus-nucleus (AA) complex optical potential (or, in general, nucleus-nucleus interactions to be used in nuclear-reaction calculations such as distorted-wave Born approximations and coupled-channels calculations) and to establish a consistent definition of local density for AA system based on the reliable G-matrix interaction having a realistic density dependence over the wide range of nucleon density consistent with the realistic nuclear-matter property.

In the present article, we have proposed new realistic complex G-matrix interactions that are calculated starting from a free-space NN interaction called the ESC force. Inclusion of the three-body force makes the saturation curve in nuclear matter more realistic up to the high-density region. According to the successful application to the proton-nucleus elastic scattering over the wide range of incident energies and target nuclei presented in this article, we may have a good reason to expect the present new G-matrix interaction to be a promising candidate of the effective interactions for our final goal mentioned above. In fact, we have already tested the present G matrix in some cases of nucleus-nucleus scattering systems with a considerable success. A full detailed analysis of application to the nucleus-nucleus systems is underway by the present authors and the results will be reported in a forthcoming article.

ACKNOWLEDGMENTS

The authors thank professor Y. Iseri and doctor M. Takashina for valuable discussions about the theoretical framework for calculating the LS part of the FMP and doctor K. Ogata for discussions about local approximation of the exchange part of FMP. T. Furumoto is supported by the Japan Society for the Promotion of Science for Young Scientists.

[1] F. A. Brieva and J. R. Rook, Nucl. Phys. **A291**, 299 (1977).
[2] F. A. Brieva and J. R. Rook, Nucl. Phys. **A291**, 317 (1977).
[3] F. A. Brieva and J. R. Rook, Nucl. Phys. **A297**, 206 (1978).
[4] L. Rikus and V. V. Geramb, Nucl. Phys. **A426**, 496 (1984).
[5] J. P. Jeukenne, A. Lejeune, and C. Mahaux, Phys. Rev. C **16**, 80 (1977).
[6] E. Bauge, J. P. Delaroche, and M. Girod, Phys. Rev. C **58**, 1118 (1998).
[7] N. Yamaguchi, S. Nagata, and T. Matsuda, Prog. Theor. Phys. **70**, 459 (1983).
[8] N. Yamaguchi, S. Nagata, and J. Michiyama, Prog. Theor. Phys. **76**, 1289 (1986).
[9] K. Amos, P. J. Dortmans, H. V. von Geramb, S. Karataglidis, and J. Raynal, Adv. Nucl. Phys. **25**, 275 (2000).
[10] M. E.-A. Farid and G. R. Satchler, Nucl. Phys. **A438**, 525 (1985).
[11] D. T. Khoa, W. von Oertzen, and H. G. Bohlen, Phys. Rev. C **49**, 1652 (1994).
[12] D. T. Khoa, G. R. Satchler, and W. von Oertzen, Phys. Rev. C **56**, 954 (1997).
[13] T. Furumoto and Y. Sakuragi, Phys. Rev. C **74**, 034606 (2006).
[14] M. Katsuma, Y. Sakuragi, S. Okabe, and Y. Kondo, Prog. Theor. Phys. **107**, 377 (2002).
[15] D. T. Khoa, W. von Oertzen, and H. G. Bohlen, Phys. Rev. C **49**, 1652 (1994).
[16] T. A. Rijken, Phys. Rev. C **73**, 044007 (2006).
[17] T. A. Rijken and Y. Yamamoto, Phys. Rev. C **73**, 044008 (2006).
[18] I. E. Lagaris and V. R. Pandharipande, Nucl. Phys. **A359**, 349 (1981).
[19] R. B. Wiringa, V. Fiks, and A. Fabrocini, Phys. Rev. C **38**, 1010 (1988).
[20] M. Baldo, I. Bombaci, and G. F. Burgio, Astron. Astrophys. **328**, 274 (1997).
[21] T. Kasahara, Y. Akaishi, and H. Tanaka, Prog. Theor. Phys. Suppl. **56**, 96 (1974).
[22] J. W. Negele and D. M. Vautherin, Phys. Rev. C **5**, 1472 (1972).
[23] X. Campi and A. Bouyssy, Phys. Lett. **B73**, 263 (1978).
[24] D. T. Khoa, Phys. Rev. C **63**, 034007 (2001).
[25] J. W. Negele and K. Yazaki, Phys. Rev. Lett. **47**, 71 (1981).
[26] M. Kamimura, Nucl. Phys. **A351**, 456 (1981).
[27] J. W. Negele, Phys. Rev. C **1**, 1260 (1970).
[28] J. J. Menet, E. E. Gross, J. J. Malanify, and A. Zucker, Phys. Rev. C **4**, 1114 (1971).
[29] A. Ingemarsson, J. Nyberg, P. U. Renberg, O. Sundberg, R. F. Carlson, A. Auce, R. Johansson, G. Tibell, B. C. Clark, L. K. Kerr *et al.*, Nucl. Phys. **A653**, 341 (1999).
[30] A. Auce, A. Ingemarsson, R. Johansson, M. Lantz, G. Tibell, R. F. Carlson, M. J. Shachno, A. A. Cowley, G. C. Hillhouse, N. M. Jacobs *et al.*, Phys. Rev. C **71**, 064606 (2005).
[31] M. Ieiri, H. Sakaguchi, M. Nakamura, H. Sakamoto, H. Ogawa, M. Yosoi, T. Ichihara, N. Isshiki, Y. Takeuchi, H. Togawa *et al.*, Nucl. Instrum. Methods Phys. Res. A **257**, 253 (1987).
[32] K. Strauch and F. Titus, Phys. Rev. **103**, 200 (1956).
[33] H. O. Meyer, P. Schwandt, W. W. Jacobs, and J. R. Hall, Phys. Rev. C **27**, 459 (1983).
[34] A. Ingemarsson, O. Jonsson, and A. Hallgren, Nucl. Phys. **A319**, 377 (1979).
[35] J. R. Comfort, G. L. Moake, C. C. Foster, P. Schwandt, and W. G. Love, Phys. Rev. C **26**, 1800 (1982).
[36] H. Sakaguchi, M. Nakamura, K. Hatanaka, A. Goto, T. Noro, F. Ohtani, H. Sakamoto, H. Ogawa, and S. Kobayashi, Phys. Rev. C **26**, 944 (1982).
[37] C. Rolland, B. Geoffrion, N. Marty, M. Morlet, B. Tatischeff, and A. Willis, Nucl. Phys. **80**, 625 (1966).
[38] A. Nadasen, P. Schwandt, P. P. Singh, W. W. Jacobs, A. D. Bacher, P. T. Debevec, M. D. Kaitchuck, and J. T. Meek, Phys. Rev. C **23**, 1023 (1981).
[39] P. Schwandt, H. O. Meyer, W. W. Jacobs, A. D. Bacher, S. E. Vigdor, M. D. Kaitchuck, and T. R. Donoghue, Phys. Rev. C **26**, 55 (1982).
[40] H. Seifert, J. J. Kelly, A. E. Feldman, B. S. Flanders, M. A. Khandaker, Q. Chen, A. D. Bacher, G. P. A. Berg, E. J. Stephenson, P. Karen *et al.*, Phys. Rev. C **47**, 1615 (1993).
[41] K. Kwiatkowski and N. S. Wall, Nucl. Phys. **A301**, 349 (1978).
[42] E. Hagberg, A. Ingemarsson, and B. Sundqvist, Phys. Scr. **3**, 245 (1971).
[43] L. Lee, T. E. Drake, S. S. M. Wong, D. Frekers, R. E. Azuma, L. Buchmann, A. Galindo-Uribarri, J. D. King, R. Schubank, R. Abegg *et al.*, Phys. Lett. **B205**, 219 (1988).